

Supplementary Information:

Multiscale flow in an electro-hydrodynamically driven oil-in-oil emulsion

Atul Varshney,^{*ab} Smita Gohil,^b Mayur Sathe,^c Seshagiri Rao R V,^d J.

B. Joshi,^e S. Bhattacharya,^b Anand Yethiraj,^{*df} and Shankar Ghosh^{*b}

^a*Department of Physics of Complex Systems,*

Weizmann Institute of Science, Rehovot 76100, Israel

^b*Department of Condensed Matter Physics and Materials Science,*

Tata Institute of Fundamental Research, Homi Bhabha Road, Mumbai 400 005, India

^c*Cain Department of Chemical Engineering,*

Louisiana State University, LA 70803 USA

^d*TIFR Centre for Interdisciplinary Sciences,*

Osman Sagar Road, Narsingi, Hyderabad 500 075, India

^e*Homi Bhabha National Institute, Anushaktinagar, Mumbai 400 094, India*

^f*Department of Physics and Physical Oceanography, Memorial University,*

St. John's, Newfoundland Labrador, Canada, A1B 3X7

Materials and Methods

The materials constants are listed in Supplementary Table 1. An external time-invariant electric field (E) was applied across the parallel plate. The flow induced stresses at the surface of the top ITO electrode was measured by a commercial rheometer (Anton Paar; MCR301). The strain in the rheometer is kept at a value of 0.1%. The system was simultaneously imaged from the bottom with a high-speed camera (PCO 1200s) attached with a long working distance microscope objective. For each value of E , a time series of the shear stress (τ) was recorded from the rheometer measurements (for about 4 hours with a 2 second time interval between data points). Simultaneously, a video of the resulting droplet motion was also recorded by the fast camera at a frame rate of 60 frames/sec. The images were acquired for about 10 seconds.

Liquid	Viscosity (η) Pa · s	Density (ρ) Kg/m ³	Dielectric constant (ϵ)	Conductivity (σ) S/m
Castor Oil	0.71	960	4.50	7.3×10^{-10}
Silicone Oil	1	760	2.75	3.6×10^{-10}

Interfacial tension $\gamma=3$ mN/m

Supplementary Table 1: Table of materials constants

Supplementary Movie 1:

The movie shows the onset of droplet motion as the field is turned on from 0 to $6.7 \text{ V}/\mu\text{m}$. It is recorded at 60 fps and displayed at 15 fps .

Supplementary Movie 2:

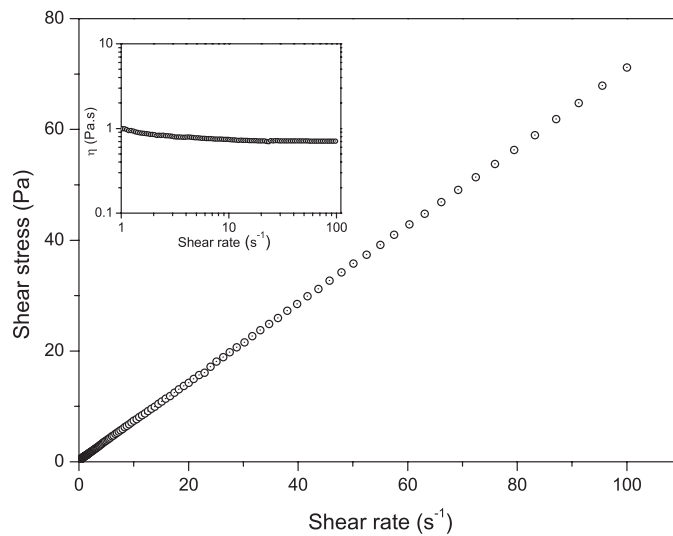
The movie shows the convection of droplets at $E = 12 \text{ V}/\mu\text{m}$. It is recorded at 60 fps and displayed at 15 fps .

Supplementary Movie 3:

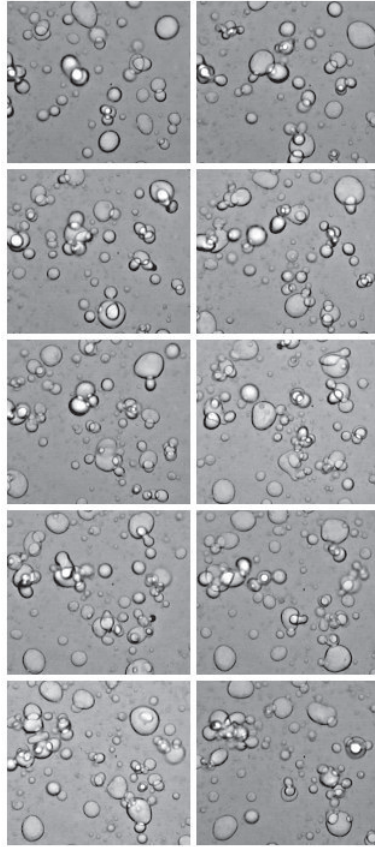
The movie, acquired at 116 fps in a small area near the cantilever, shows convection: droplets that go in and out of focus with a period of approximately 0.5 second. Large droplets rotate, while smaller ones revolve around the large one.

Supplementary Movie 4:

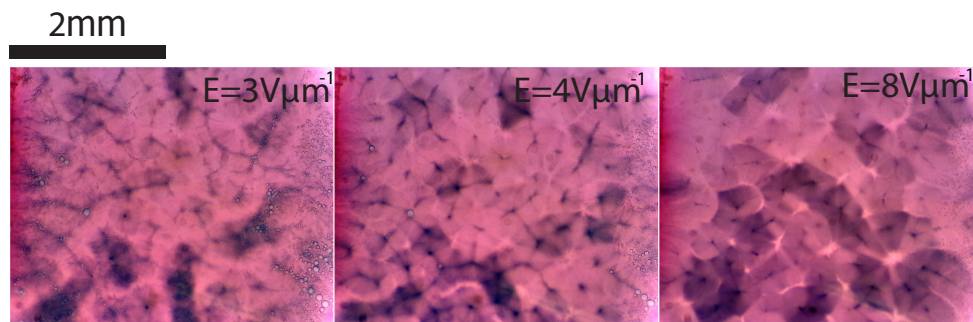
The movie shows the mixing of dye in the system for $E = 1 \text{ V}/\mu\text{m}$ (left) and $5 \text{ V}/\mu\text{m}$ (right). It is recorded at 0.2 fps and displayed at 15 fps .



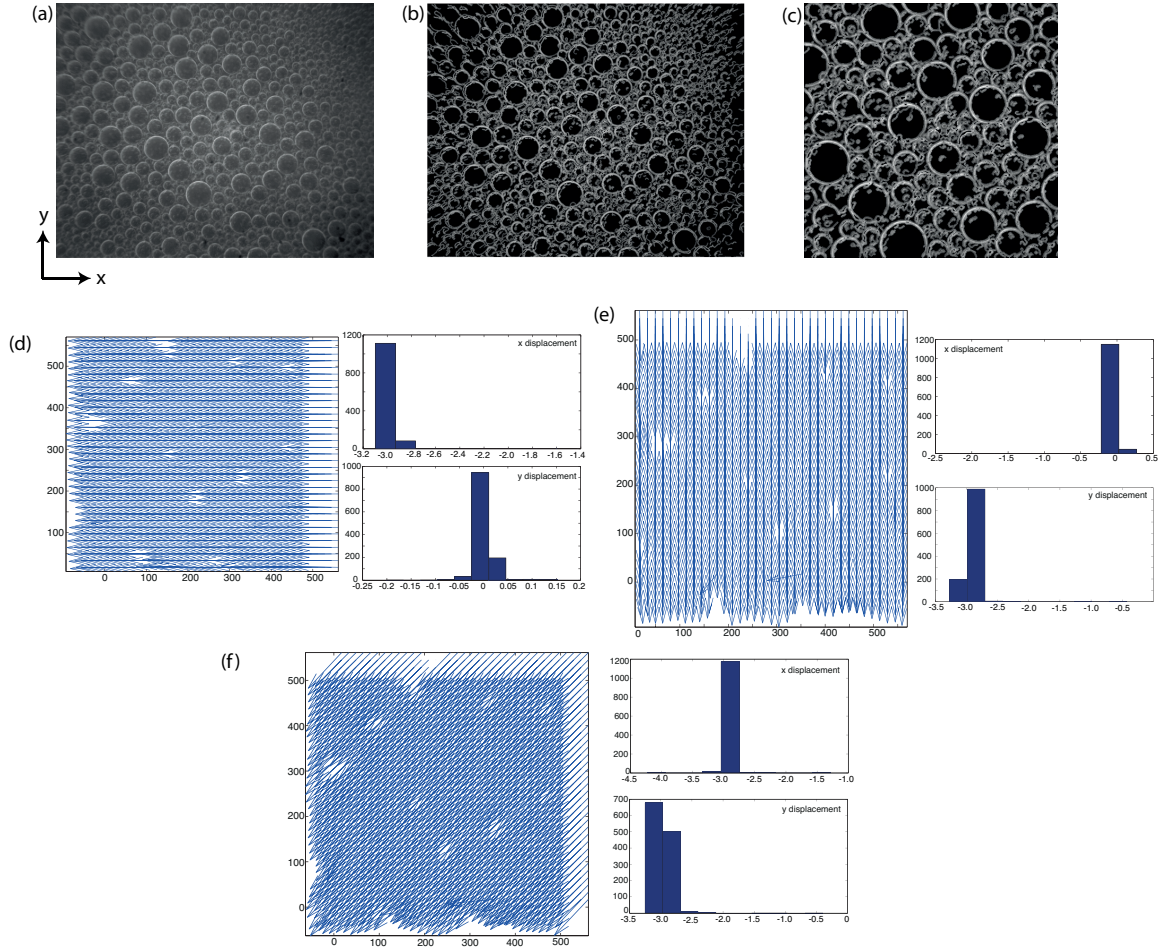
Supplementary Figure 1: Flow curve, shear stress versus shear rate, for the oil-in-oil emulsion. Inset shows the dependency of viscosity of emulsion on the shear rate. In the absence of an external field, the emulsion is Newtonian, exhibiting a clean, linear dependence of stress on shear rate.



Supplementary Figure 2: Time sequence micrographs obtained at $E = 5 \text{ V}/\mu\text{m}$. The effect of electric field induced hydrodynamic flow is manifested in the deformation of the droplets while the effect of accumulation of surface charges is evident for droplets of larger sizes which split into smaller ones.



Supplementary Figure 3: Snapshots of the system at different electric field values (marked on top right). Each image at a given E is a stacked sum of 100 images (each taken at 30 ms time apart). With increasing field, these clusters become more space filling, though their internal structure does not evolve appreciably, as shown by the dark regions. The experimental details are provided in the section on mixing.



Supplementary Figure 4: (a) A typical example of a grey scale image obtained from the experiment. A high pass filter was used to detect the edges. The resulting thresholded image is shown in (b). To check the validity of the PIV algorithm implemented in the analysis we choose two segments of threshold image (576×576 pixels) with slight shift in location. An example of the segment used is shown in (c). The results, velocity vectors and the displacement histograms for $dx = -3$ pixels, $dy = 0$; $dx = 0$, $dy = -3$ pixels, and $dx = dy = -3$ pixels are shown in (d), (e) and (f), respectively. A single pixel corresponds to $\sim 2.7 \mu\text{m}$ in length.

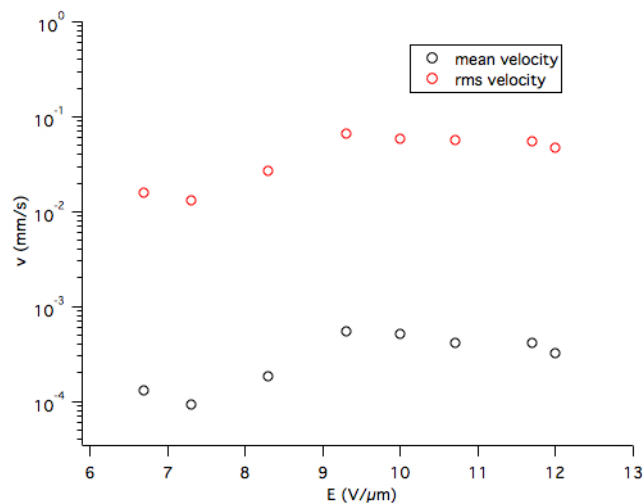
Particle Image Velocimetry

Since the particle image velocimetry (PIV) technique relies upon ensemble movement rather than tracing individual particles, we ventured into calculating the drop edge velocity measurement using the same technique. The velocity components calculated using drop images differ from continuous phase by the magnitude of local slip velocity. However, statistical similarity between dispersed and continuous phase velocity distribution is expected since interfacial area is high enough to ensure that local momentum transfer reaches equilibrium. The calculation of displacement of droplets

ensemble is accurate if (i) drops are smaller than PIV interrogation area, (ii) drop velocity is similar inside each interrogation area, and (iii) drop displacement is less than half of PIV interrogation area size. We ensured that all three criteria are satisfied for the reported PIV data.

To demonstrate the accuracy of PIV processing on drop images, we took a piece of the actual drop image, applied a high pass filter to detect drop edges and generated artificially shifted image pairs with known X and Y displacements, as shown in Supplementary Fig. 4. A pixel grid of size $22 \times 22 \mu\text{m}^2$ was used for cross-correlation of successive frames. About 200 frames are analyzed at each electric field value. The PIV software package [1] developed for MATLAB is used for the analysis. The following figures show that the PIV algorithm is able to accurately discern the drop movements throughout the image. A few spurious vectors were generated in regions with no drops, which were removed by the outlier analysis.

Tests in the limiting case of small velocities show that this method gives results comparable to the droplet centroid tracking. The power spectra computed from stress fluctuations as measured by the rheometer and the velocity fluctuations as measured by PIV exhibit scaling that is mutually consistent. The good agreement between the two suggests that ambiguity in the velocity magnitude as measured by the PIV is not significant. The mean and rms velocities obtained from the PIV analysis are shown as a function of electric field in Supplementary Fig. 5.



Supplementary Figure 5: Variation of mean and rms velocities with electric field E in the active regime. The velocities are obtained from PIV analysis.

[1] W. Thielicke and E. J. Stamhuis, Journal of Open Research Software **2** (2014), ISSN 2049-9647.